

Manipulation of single cells inside nanoliter water droplets using acoustic forces

Cite as: Biomicrofluidics 14, 064112 (2020); doi: 10.1063/5.0036407

Submitted: 5 November 2020 · Accepted: 8 December 2020 ·

Published Online: 18 December 2020



View Online



Export Citation



CrossMark

Michael S. Gerlt,^{1,a)} Dominik Haidas,² Alexandre Ratschat,¹ Philipp Suter,¹ Petra S. Dittrich,² and Jürg Dual¹

AFFILIATIONS

¹Department of Mechanical and Process Engineering, ETH Zurich, Institute for Mechanical Systems (IMES), Tannenstrasse 3, CH-8092 Zurich, Switzerland

²Department of Biosystems Science and Engineering, ETH Zurich, Bioanalytics Group, Mattenstrasse 26, CH-4058 Basel, Switzerland

^{a)}**Author to whom correspondence should be addressed:** gerlt@imes.mavt.ethz.ch

ABSTRACT

Droplet microfluidics enables high-throughput screening of single cells and is particularly valuable for applications, where the secreted compounds are analyzed. Typically, optical methods are employed for analysis, which are limited in their applicability as labeling protocols are required. Alternative label-free methods such as mass spectrometry would broaden the range of assays but are harmful to the cells, which is detrimental for some applications such as directed evolution. In this context, separation of cells from supernatant is beneficial prior to the analysis to retain viable cells. In this work, we propose an in-droplet separation method based on contactless and label-free acoustic particle manipulation. In a microfluidic chip, nanoliter droplets containing particles are produced at a T-junction. The particles are trapped in the tip of the droplet by the interplay of acoustic forces in two dimensions and internal flow fields. The droplets are subsequently split at a second T-junction into two daughter droplets—one containing the supernatant and the other containing the corresponding particles. The separation efficiency is measured in detail for polystyrene (PS) beads as a function of droplet speed, size, split ratio, and particle concentration. Further, single-bead (PS) and single-cell (yeast) experiments were carried out. At a throughput of 114 droplets/min, a separation efficiency of $100\% \pm 0\%$ was achieved for more than 150 droplets. Finally, mammalian cells and bacteria were introduced into the system to test its versatility. This work demonstrates a robust, non-invasive strategy to perform single yeast cell-supernatant sampling in nanoliter volumes.

Published under license by AIP Publishing. <https://doi.org/10.1063/5.0036407>

I. INTRODUCTION

Cell analysis and screening by cytometry are routinely performed in many biological and diagnostic applications. While flow cytometry is extraordinarily fast and powerful for the characterization of cell number, size, or surface proteins, standard cytometry instruments are not capable of analyzing secreted compounds like proteins, metabolites, or signaling factors. Droplet microfluidics can address this limitation by encapsulating cells in small nanoliter (nl) to picoliter (pl) compartments, where they are subjected to prescribed conditions and secreted biomolecules accumulate.¹

Consequently, the enriched molecules can be analyzed at high sensitivity, commonly using fluorescence assays.^{2–5} One important application of droplet-based cytometry is, among many others, directed evolution—a well-established methodology in the field of protein engineering. Directed evolution relies on the creation of a

library of gene variants in cells or cell-free systems and subsequent selection of a defined phenotype, e.g., the brightness of proteins or catalytic activity of enzymes.^{6–8} The use of fluorescence assays, however, requires a fluorogenic reaction or a labeling procedure and, therefore, limits the applicability of droplet microfluidics for cell analysis. We are developing an alternative system using label-free detection by mass spectrometry (MS). Recent studies demonstrated that droplet microfluidics could be interfaced with mass spectrometers to detect cells and secreted analytes.^{1,9} Nevertheless, since MS is a destructive method, separation of dissolved compounds and cells is essential to maintain the cells' viability and obtain a signal devoid of background noise from cell constituents. Withdrawal of particles or cells from droplets is also beneficial for many multistep biochemical assays.¹⁰ For screening applications such as directed evolution, special requirements need to be met

regarding the separation procedure. Single cells need to be encapsulated inside nanoliter droplets and subsequently split with a separation efficiency (SE) of 100% at high throughput. Several methods have been developed for particle manipulation inside nanoliter droplets based on magnetic,^{10–12} dielectric,¹³ hydrodynamic,^{14–16} or acoustic forces,^{17–29} and more recently, for in-droplet separation of biomolecules.³⁰ However, none of the mentioned publications currently fulfills the need for label-free high-throughput screening. Magnetophoresis requires particle labeling, dielectrophoresis operates at low flow rates, hydrodynamic forces are passive, and acoustophoresis has not been shown to reproducibly separate particles at a SE of 100%.³¹ In this work, we push the limits of acoustophoresis to achieve single-particle separation with an efficiency of 100% at high throughput.

Acoustophoresis is a contactless particle manipulation method based on the scattering of ultrasonic waves on the particle surface. Acoustophoretic forces depend on particle size and density difference to its surrounding medium. Acoustophoresis is label-free,³² flexible in design,³³ and biocompatible.³⁴ We exploit acoustophoresis to manipulate particles and cells inside passing droplets before the droplets are split into daughter droplets at a T-junction. In contrast to Fornell *et al.*,^{22,26,27} our design contained two perpendicular outlet channels with different widths for higher separation efficiencies. Using numerical and experimental investigations, we found an optimal side-channel width of 90 μm . The devices were characterized with polystyrene (PS) particles by varying the droplet speed, size, split ratio, and particle concentration, to allow for improved accessibility and simplified adaptability of our device to the reader's needs. Acoustofluidic devices already showed outstanding performance concerning separation efficiency and throughput.^{26,31} With our

device design, we were able to show an even higher separation efficiency while doubling the flow rate and lowering the droplet volume, which is of interest for rare cell separation. We achieve these high separation efficiencies with an interplay of acoustic forces in two dimensions and droplet internal flow fields.

Based on our thorough device characterization, the parameter set has been optimized for the experimental manipulation of yeast cells. To the best of our knowledge, this is the first demonstration of single-cell manipulation in nanoliter droplets using acoustic forces. We were able to maintain a SE of 100% in more than 100 droplets at a high throughput of 114 droplets/min. Finally, we applied our method to HeLa cells (mammalian) and *E. coli* (bacteria). Since the intra-droplet manipulation of bacteria and mammalian cells has not yet been reported in the literature, our device broadens the applicability of acoustofluidic particle manipulation in microscale droplets.

II. OPERATING PRINCIPLE

The acoustofluidic chip is capable of on-chip droplet production, particle manipulation inside droplets, and droplet splitting (Fig. 1). A T-junction was chosen for droplet production in oil since it is very well understood and optimal to achieve slug flow (squeezing regime) at various flow rates.^{35–38} In this regime, only a very thin (sub- μm) oil film develops between droplet and channel wall.³⁹ Therefore, the oil film does not need to be considered for the acoustics, which eases the modeling of the system.

After droplet production, particles are manipulated inside the droplet by bulk acoustic waves (BAWs). These waves are generated by a piezoelectric transducer (piezo), which is glued to the backside of the chip. The force acting on small (with respect to the acoustic

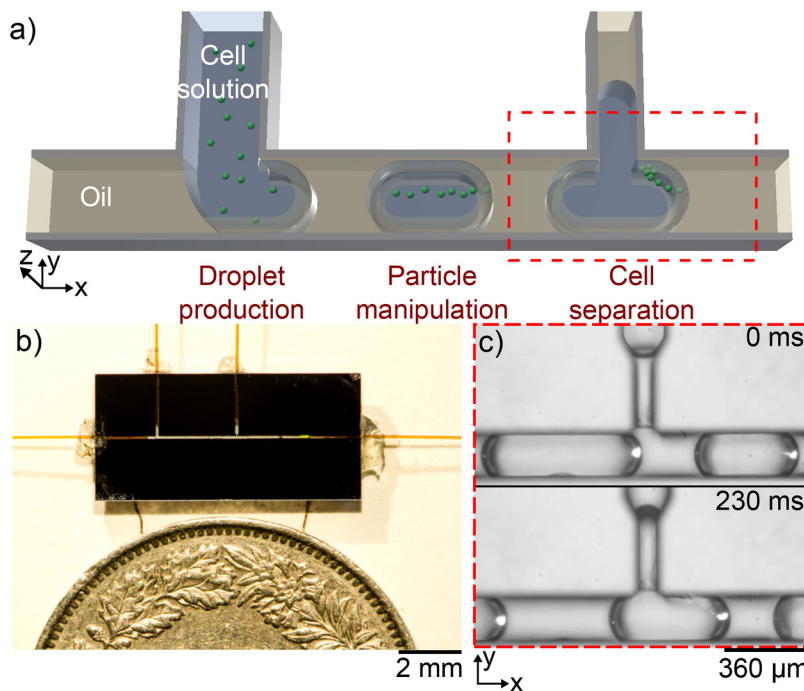


FIG. 1. Working principle of cell separation in nanoliter droplets. (a) Sketch of the design. (b) Photograph of the acoustofluidic chip. Underneath the chip lies a Swiss franc coin. (c) Micrograph series of a typical separation experiment (5 μm fluorescent polystyrene particles in white). The piezo was excited at 3.7 MHz with 13 Vpp. The droplets contained 93 ± 9 particles and flowed at a speed of 2 mm s^{-1} .

wavelength) particles is called acoustic radiation force (ARF). For an inviscid fluid, it is given by the negative gradient of the Gorkov potential⁴⁰

$$\mathbf{F}_{\text{rad}} = -\nabla U, \quad (2.1)$$

which can be expressed as

$$U = \frac{4}{3}\pi r^3 \left(\frac{1}{2} \langle p \rangle^2 \frac{f_0}{c^2 \rho} - \frac{3}{4} \rho f_1 \langle v \rangle^2 \right), \quad (2.2)$$

with the particle radius r , the incident acoustic pressure field p , the incident acoustic velocity field v , the fluid speed of sound c , the density of the fluid ρ , the monopole f_0 , and the dipole f_1 scattering coefficients. $\langle x \rangle$ denotes time averaging $\langle x \rangle = 1/T \int_0^T x dt$.

The average acoustic energy density (\bar{E}_{ac}) is given as⁴¹

$$\bar{E}_{ac} = \frac{1}{V} \int_V \left(\frac{1}{2} \rho \langle v \rangle^2 + \frac{1}{2} \kappa \langle p \rangle^2 dV \right), \quad (2.3)$$

with compressibility κ and volume V .

Droplets flowing through a microchannel develop complex internal flow fields.^{14,42,43} They are mainly caused by the no-slip boundary condition (BC) at the channel walls and by oil surpassing the droplets through corner gutters.³⁹ Corner gutters are small gaps in between droplets and rectangular channel walls that appear due to surface tension. Separation of cell and supernatant can only be achieved if the ARF is stronger than the drag force resulting from the internal flow fields or if the cell is moved into a desirable flow pattern such that it is trapped in some part of the droplet.

In this work, we focus the particles in two dimensions (z- and y-direction), which is an inherent feature of our square-shaped channels. With the focus in the z-direction, we can move the particles to approximately half the droplet height. In this plane, the flow fields point toward the tip of the droplet except for small regions at the top and bottom of the droplet where recirculation zones form. The force in y-direction allows us to overcome these recirculation zones and focus the particles in the tip of the droplet, which is desirable for particle separation. Another feature of square-shaped channels is rotating streaming flows, which enable us to manipulate particles with a diameter in the range of 1 μm .⁴⁴

The droplets are split at a bifurcation during particle manipulation. Successful splitting of droplets highly depends on the capillary number and the volume of the droplet. The smaller the droplet volume, the higher needs to be the capillary number to split the droplets.^{45,46} The capillary number can be increased by higher flow rates or lower surface tension of the droplets. However, if slow flow speeds are required such as for manipulation of bacteria, droplet splitting cannot be achieved anymore.

III. MATERIALS AND METHODS

A. Device fabrication

The devices were produced using standard cleanroom processes. Microfluidic channels (180 μm depth and width) were etched into a silicon wafer (500 μm thickness) by the combination of

photolithography and inductively coupled plasma deep reactive ion etching (ICP-DRIE). High aspect ratios and straight channel walls of around 88° can be achieved using this method. A glass wafer (700 μm thickness) was anodically bonded to the silicon wafer. The wafer was diced into small rectangles (15.2 \times 7.38 mm²) utilizing a wafer saw. Fused silica capillaries (164 \pm 6 μm outer diameter, 100 \pm 6 μm inner diameter, Polymicro Technologies—Molex) were plugged into the sides of the chip and fixed with a two-component glue (5 Minute® Epoxy, Devon). A piezo (10 mm length, 1.5 mm width, 0.5 mm thickness, Pz26, Meggitt Ferroperm, Kvistgaard, Denmark) was glued to the backside of the devices. Since the piezo is smaller than the device, we used conductive epoxy (H20E, EPO-TEK®) to be able to contact the side of the piezo that is attached to the device. Additionally, H20E proved to be one of the glues with the least damping of acoustic waves. Copper cables (0.15 mm diameter) were attached to the piezo with conductive silver paste and glued to the chip with instant glue to increase the mechanical stability. The channels were silanized with a surface coating agent (Repel-silane ES, Merck) to render them hydrophobic. Therefore, we flushed the devices with Repel-silane ES, waited for 10 min, and finally flushed the chip with olive oil. This step is crucial for a monodisperse and reproducible droplet production in silicon chips.

B. Experimental setup

BAW devices are based on the generation of ultrasonic standing waves in microfluidic channels. The waves are coupled into the devices by exciting the piezo with an AC signal. Generation of the signal is achieved using a wave generator (AFG3022B, Tektronix). The impedance of the piezo varies with its excitation frequency. Since the voltage at the piezo is dependent on its impedance, it is verified using an oscilloscope (WS424, LeCroy). Water and oil flow inside the microfluidic channels are controlled by syringe pumps (neMESYS 290 N, Cetoni). The syringes were kept upright such that the outlet of the syringe is pointing downward. Thereby, particles are pushed toward the outlet of the syringe by gravity, and the number of empty droplets is reduced. Green fluorescent PS particles (5.19 μm \pm 0.14 μm , diameter, microParticles GmbH) were used for characterization experiments. Particle manipulation was observed with a self-built microscope kit (Cerna®, Thorlabs). A green LED (M505L3, Thorlabs) excites the particles via a dichroic mirror (MD515, Thorlabs). Before entering the camera, the light is filtered by an emission filter (MF535-22, Thorlabs). A high-speed camera (HiSpec1, Fastec) is used to visualize the fast in-droplet separation process. Depending on the speed of the droplets, a frame rate between 100 and 200 fps was used.

C. Standard experimental parameters

If not stated otherwise, the experiments were conducted with the following experimental parameters. The voltage at the piezo was kept constant at 13 Vpp, which is the limit of the used wave generator at the resonance of the piezo. The excitation frequency of the piezo was between 3.70 and 3.75 MHz. The optimal frequency was chosen upon visual inspection. The particle concentration was kept constant at 93 \pm 9 (mean \pm standard deviation) particles per droplet (ppd). The droplet volume before splitting was kept at 12.8 \pm 1.2 nl. The droplet speed was 2.1 mm s⁻¹. At the bifurcation,

the droplets were split into equally sized daughter droplets, meaning a split ratio of 50%. The split ratio is given as the ratio between the volume of the daughter droplet exiting to the side channel and the initial droplet volume. We utilized olive oil (CAS number 8001-25-0, Merck) as the continuous phase without surfactant.

D. Determination of the separation efficiency

Characterization of our design for in-droplet particle separation was done with fluorescent PS particles. The particles are visible in the microscope pictures, even if they are not in the focal plane. Due to the presence of particle aggregates caused by acoustophoretic focusing, we counted particles manually. The volume of the droplets was approximated by counting the number of droplets per time at a pre-set flow rate. The number of particles inside the droplets was determined by counting the particles in droplets with a very low concentration of 0.125 gl^{-1} . For other concentrations and droplet volumes, this number was linearly interpolated. The separation efficiency (SE) is defined by

$$\text{SE} = 1 - \frac{\text{PSC}}{\text{PBS}}, \quad (3.1)$$

where we used the number of particles exiting to the side channel (PSC) and the number of particles before splitting (PBS).

E. Numerical model

2D (xy) models of the chip were built and evaluated in the finite-element method software COMSOL Multiphysics version 5.4 to evaluate the influence of the continuous phase and the side channel on the Gorkov potential. A mesh study and evaluation of the perfectly matched layer (PML) size was conducted. A perfectly matched layer width of $100 \mu\text{m}$ and 15 mesh elements per wavelength turned out to be sufficient for both models (Fig. S1 in the [supplementary material](#)). The pressure acoustics module was used and evaluated in the frequency domain.

The first model was built to investigate the influence of different carrier media on particle manipulation inside droplets. A normal displacement boundary condition (BC, 10 nm amplitude) was assigned to the bottom channel wall to model the actuation by the piezoelectric element. The top and side-channel walls received an impedance BC ($Z = 19.8 \times 10^6 \text{ kg m}^{-2} \text{ s}^{-1}$). A sound soft BC was applied to all outlets (Fig. S1 in the [supplementary material](#)).

The second model was built to investigate the influence of the side channel on the Gorkov potential and, therefore, on the particle manipulation. The BCs and PML parameters were kept as described above. Additional to the first model, a side channel was introduced. The materials inside both channels were set to water. In both models, Eqs. (2.2) and (2.3) are implemented to be able to evaluate the Gorkov potential and acoustic energy density.

IV. RESULTS AND DISCUSSION

A. Influence of the continuous phase on the particle focusing

For a better understanding of the acoustic focusing inside water droplets, numerical studies were carried out. We compared the effect

of different continuous phases (fluorinated oil and olive oil) on the Gorkov potential. Olive oil ($c = 1450 \text{ m s}^{-1}$, $\rho = 910 \text{ kg m}^{-3}$) exhibited acoustic properties very close to water. As can be seen in [Fig. 2](#), the resonance frequencies for the $\lambda/2$ -mode (half an acoustic wavelength in the channel) in water and olive oil are similar. Therefore, the minimum of the Gorkov potential stretches along the center of the whole channel including the droplet. The fluorinated oil 3M™ Novec™ HFE 7500 (HFE, $c = 659 \text{ m s}^{-1}$, $\rho = 1621 \text{ kg m}^{-3}$) exhibited acoustic properties different from water. The frequencies to excite the $\lambda/2$ -mode inside the channel and in the droplet are 2511 kHz apart compared to 46 kHz with olive oil. At the resonance frequency of the water droplet, the Gorkov potential is strong in the center of the droplet. However, the ARF gets weak and changes its direction toward the rear and the tip of the droplet ([Fig. 2](#)).

Since the microfluidic channels of our devices exhibit a square shape, particles are focused in two dimensions (y and z) when turning on the ultrasound. The flow field at the center (y-direction) of the droplet at a plane of half its height (z-direction) is pointing toward the tip of the droplet.¹⁴ If the force in y-direction at the tip of the droplet is strong enough to retain particles from entering the circulating vortices at the top and bottom of the droplet, the particles remain in the tip of the droplet. This is essential for the cell-supernatant separation since particles at the tip of the droplet do not enter the side channel (Video 1 in the [supplementary material](#)). As shown in [Fig. 2](#), the clumping of particles at the tip of the droplet is achieved for olive oil as the continuous phase. If HFE is used, the majority of the acoustic radiation force is pointing in the x-direction. Hence, the force in the y-direction at the tip of the droplets is not strong enough to prevent particles from entering the circulation zones. Once the particles enter the circulation zones, they are transported toward the center of the droplet, where they begin to travel back to the tip. Therefore, they cannot be prevented from entering the side channel at the splitting junction leading to a low SE. Fornell *et al.* discussed this phenomenon for rectangular channels. Here, particles can only be focused in a line with olive oil as the continuous phase. In the case of HFE, they report the same difficulties for particle focusing. However, their analysis is based on a 3D model.²⁹ With our computationally cheap 2D model, devices can be analyzed and optimized much more efficiently, making them more accessible to a broad audience.

For acoustic particle manipulation inside droplets, matching acoustic properties of droplet and carrier phase media is essential.

B. Important device design parameters

To achieve optimal performance, we varied the design of the acoustofluidic chips. The three parameters we discuss here are the width of the side channel, the width of the main channel, and the angle between the side and main channel.

For bifurcations with an angle of 45°, the SE [Eq. (3.1)] decreased significantly compared to the design with a 90° bifurcation ([Fig. S2](#) and Video 2 in the [supplementary material](#)). Such angles lead to sharp edge-like structures, which present a trapping site in acoustofluidic applications.⁴⁷ This could explain SE below 100% in similar studies that utilize a bifurcation with 45° angles^{22,27} or small structures that under excitation could act as trapping sites.^{21,26}

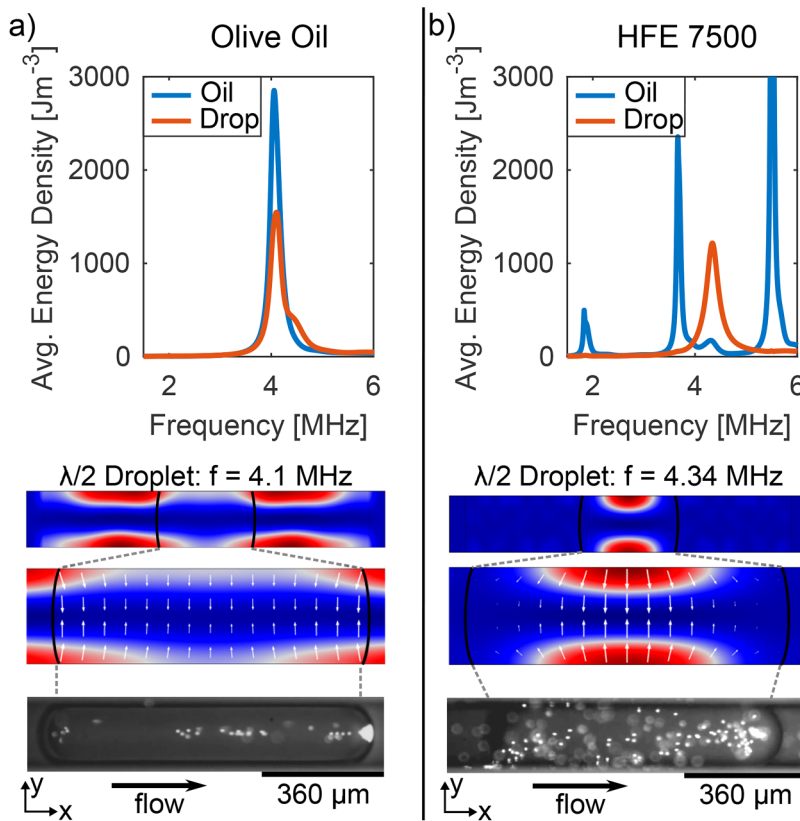


FIG. 2. Influence of the continuous phase and droplet properties on particle manipulation for (a) olive oil and (b) HFE 7500 as the carrier medium. The graphs on the top of the figure show the influence of the frequency on the average acoustic energy density in the continuous phase and droplet. The two pictures in the middle show the distribution of the Gorkov potential at an optimal frequency with respect to the average acoustic energy density in the droplet. The ARF is plotted as white arrows for the enlarged region of the droplet. The length of the arrows was set proportional with a scale factor of 4000. Cells migrate to the minimum of the potential (blue). The pictures on the bottom show the manipulation of 5 μm fluorescent PS particles in droplets with a volume of 29 ± 0.77 nl at a flow speed of 2 mm s^{-1} at an excitation frequency of 3.9 MHz. Olive oil produces a favorable acoustic field for particle manipulation inside nanoliter droplets.

Another important parameter is the width of the side channel. We numerically investigated side-channel widths between 1 and 180 μm (Fig. S3 in the [supplementary material](#)). The results suggest that the smallest side-channel width leads to the most homogeneous Gorkov potential along the whole channel. However, if the chosen width is too small, stable splitting of the droplets cannot be guaranteed. This could be due to the high pressure drop between the side and main channel, which is difficult to control. Of all the tested side-channel widths (30, 60, and 90 μm), only the 90 μm wide side channel shows sufficiently stable droplet splitting throughout the experiments.

The third and final parameter that was varied is the width of the main channel. A smaller main channel width has two positive effects. First, smaller droplets can be produced, which decreases the dilution of the secreted molecules. Second, a smaller channel width demands higher frequencies to achieve the $\lambda/2$ -mode, which would lead to higher forces [Eq. (2.2)]. Therefore, devices with rectangular channels of 100 μm in width and 180 μm in height were tested. In contrast to square-shaped channels, particle manipulation in the height and width direction is decoupled for these rectangular channels. We were able to observe particle manipulation at the same frequency as with the square-shaped channels (3.75 MHz). At higher frequencies, no further particle manipulation could be observed even at higher voltages. Therefore, the particles were only focused in the z-direction. This leads to particle accumulation in the back of the droplet. Here, particles can escape to the side channel

([Video 3 in the supplementary material](#)). Since a simultaneous manipulation along channel height and width could not be performed with the utilized transducer, this design was omitted for further experiments. Considering the previous findings, devices with a 90° bifurcation, 90 μm side channel width, and 180 μm main channel width were used for further experiments.

C. Device characterization

Depending on the experiment, the goal of particle separation in droplets can be manifold. In this section, the influence of various experimental parameters on the SE is presented. In [Fig. 3](#), an overview of all experiments with 5 μm green fluorescent PS beads is given. Increasing the speed of the droplet leads to stronger drag forces from the internal flow fields. These drag forces counteract the particle accumulation in the tip of the droplet leading to a decrease in SE. The SE decreases from $99.9\% \pm 0.1\%$ at 2 mm s^{-1} to $83.8\% \pm 7.1\%$ at 4 mm s^{-1} , illustrating the influence of the internal flow fields. By varying the ratio between oil and water flow rate, the droplet volume was decreased to 8.1 ± 0.5 nl. Below this size, splitting of the droplets could not be achieved. For a droplet volume of about 12.8 ± 1.2 nl, the droplet speed could not be faster than 2 mm s^{-1} if an average SE above 99% was desired. For droplet volumes of 8.1 ± 0.5 nl, the flow speed can be doubled to 4 mm s^{-1} while maintaining a high SE of $99.5\% \pm 0.5\%$ [[Fig. 3\(a\)](#)]. The achieved separation efficiency is crucial for rare cell separation and

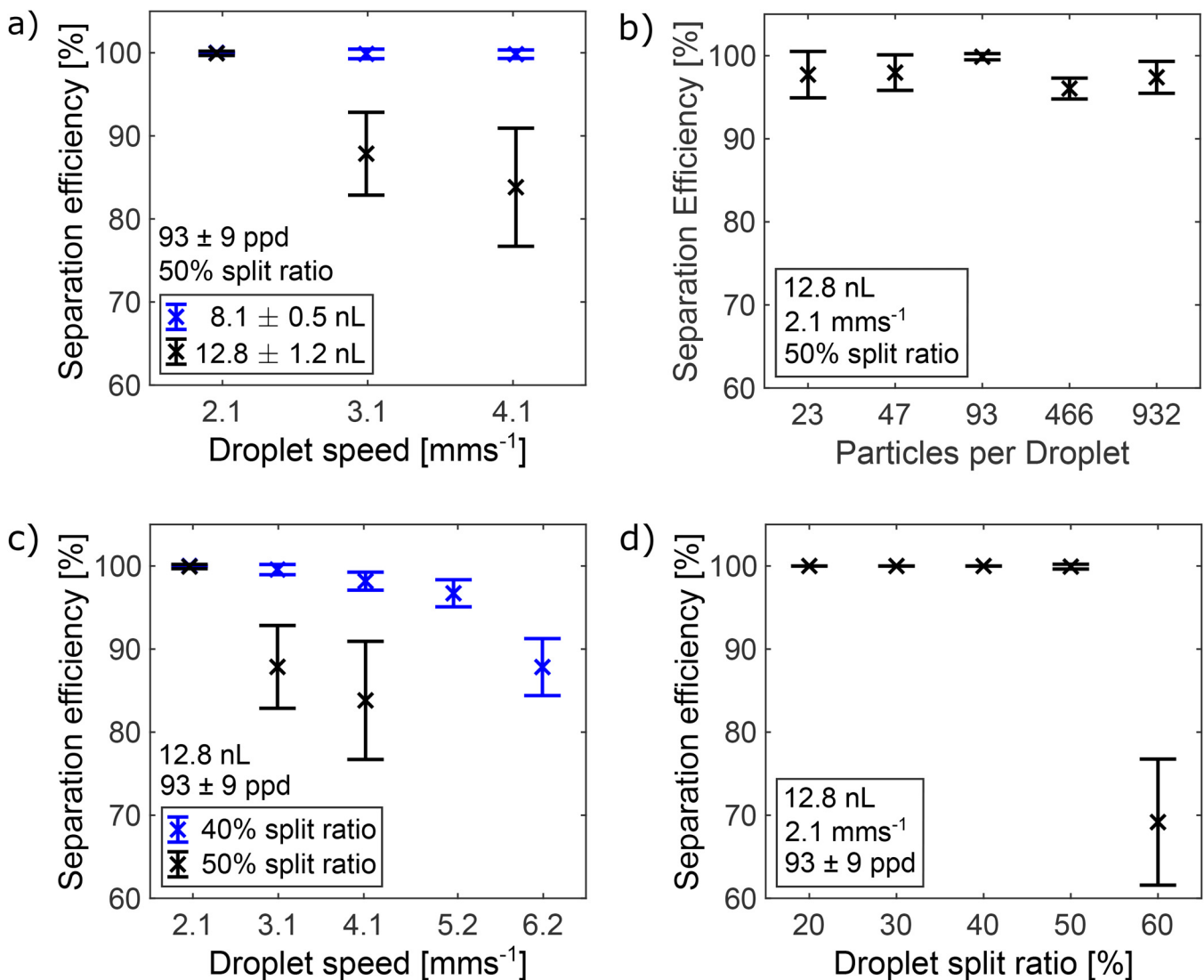


FIG. 3. Influence of various experimental parameters on the separation efficiency (SE) for PS particles. The cross and error bar correspond to the mean value and the standard deviation of the SE, respectively. 30 droplets were evaluated for each data point. (a) Influence of the droplet speed and volume on the SE. With increasing droplet speed, the standard deviation increases significantly due to the stronger internal flow fields. However, the SE still is $83.8\% \pm 7.1\%$ at 4.1 mm s^{-1} . A decrease in droplet volume from 12.8 to 8.1 nL led to a SE of $95.9\% \pm 0.5\%$ even at 4.1 mm s^{-1} droplet speed. (b) Influence of the particle concentration on the SE. The number of particles inside droplets could be determined with an error of approximately 10%. The SE can be maintained at an average value of above 97% even at high concentrations of 932 ppd. (c) Influence of the split ratio on the SE. If the split ratio is lowered to 40%, the SE is $87.8\% \pm 3.4\%$ for droplet speeds of 6.2 mm s^{-1} . (d) On maintaining a constant droplet speed of 2 mm s^{-1} , a significant drop in SE can be observed above a split ratio of 50%.

demonstrates a significant improvement over current acoustofluidic devices.²⁶ For a lower droplet volume, the size of the recirculation zones at the top and bottom of the droplets is reduced. Therefore, less force is needed to keep the particles in the tip of the droplet, which explains the high SE.

Even for very high concentrations of more than 900 ppd, a SE of $97.4\% \pm 1.9\%$ can be achieved [Fig. 3(b)]. At such high concentrations, there is not enough space for all particles to be trapped in

the tip of the droplet. Therefore, particles that enter the flow fields from the top and bottom of the droplet are transferred backward and can escape into the side channel (Video 4 in the [supplementary material](#)). Nevertheless, despite the high particle concentration, our method was able to maintain an average separation efficiency above 97%, which, given the novelty of our achievement, might be of additional interest. At low concentrations of around 23 particles per droplet, only a few particles escape into the side channel

(1 particle every third droplet). However, these particles have a big influence on the standard deviation, which increased significantly ($97.2\% \pm 2.8\%$). The droplet split ratio can be adjusted by connecting syringe pumps to the outlets to change their respective flow rates. If the split ratio is decreased by 10%, the droplet speed can be increased up to 6 mm s^{-1} , while still maintaining an average SE above 87% with a standard deviation of 3.4% [Fig 3(c)]. Since less fluid is extracted at the side outlet, particles inside the droplet are more prone to follow into the main outlet. On the other hand, if the split ratio is increased by 10%, the SE drops to $69.1\% \pm 7.6\%$ even at a low flow speed of 2 mm s^{-1} [Fig. 3(d)]. With these characterizations, we define an optimal working range of our device, to make it more easily accessible to a variety of research fields benefiting from reliable particle manipulation.

D. Yeast cell-supernatant separation in nanoliter droplets

In this section, we explore the applicability of the acoustofluidic chip for yeast cell-supernatant separation. Yeast cells exhibit acoustic properties very close to PS and have a similar size compared to the PS beads that have been used for device characterization.⁴⁸ In Fig. 4(a) and Video 5 in the [supplementary material](#), we show the separation of yeast cells from their supernatant in nanoliter droplets performed with the standard parameters (Sec. III C). Similar to the PS particles, the cells are trapped at the tip of the droplets. At the

bifurcation, the cells are dragged along with the droplets following the main channel. As can be seen in Fig. 4(b), the SE for yeast cells is even higher than that of the particles at flow speeds of 3 mm s^{-1} ($97.95\% \pm 1.9\%$) and 4 mm s^{-1} ($93.8\% \pm 3.1\%$). This might be due to the lower concentration of yeast cells (69 cells per droplet). However, further investigations are needed to investigate this increased SE.

While previous work demonstrated the manipulation of yeast cells inside nanoliter droplets, it is important to highlight that their separation efficiency for high-throughput applications was significantly limited.²²

E. Single-particle separation

In this section, we present experimental results for the separation of single PS beads and yeast cells in nanoliter water droplets.

To achieve single-particle encapsulation, we filled the syringe with a concentration of 0.000 625% w/v PS beads or 0.001 562 5% w/v yeast cells. Considering the device characterization (Sec. IV C), we kept the split ratio below 50% to achieve a good tradeoff between captured supernatant amount and high SE. Table I reveals that our device is capable of separating particle and supernatant reproducibly with a SE of 100% at a flow speed of 2 mm s^{-1} . Therefore, it fulfills one important criterion for directed evolution.

To evaluate the limits of single-particle manipulation, the droplet flow speed has been increased while keeping the additional experimental parameters constant. As expected and elaborated in

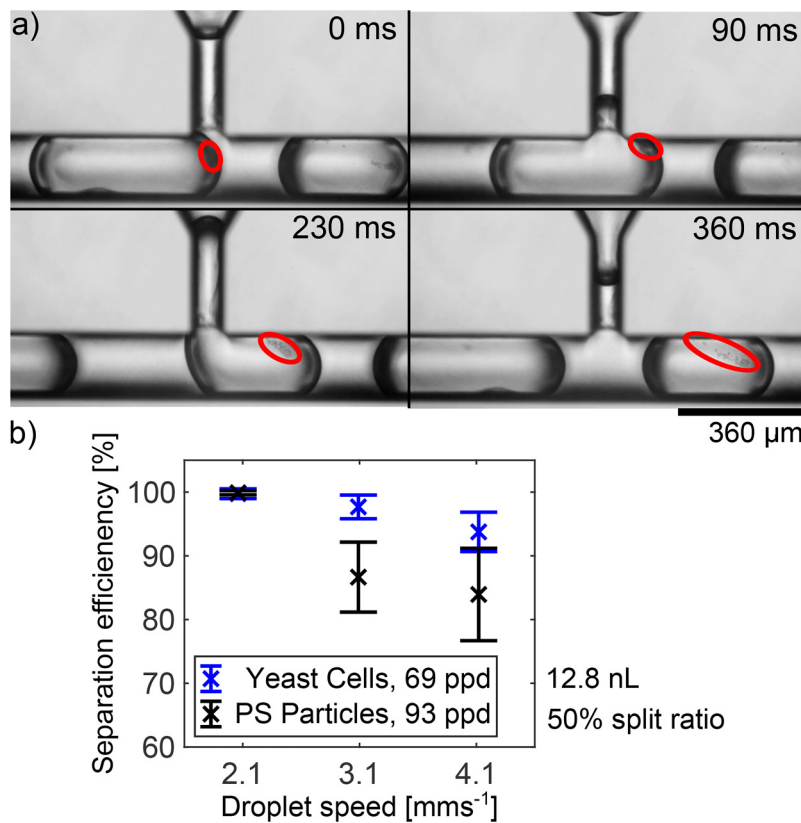


FIG. 4. Yeast cell separation in nanoliter droplets. (a) Micrograph series of the separation process. Upon manipulation, the yeast cells (inside red ellipse) have similar trajectories as the PS particles. (b) Influence of droplet speed on SE. The graph shows a comparison of yeast cells (blue) and PS particles (black). The number and the black cross corresponds to the mean value of the SE for every experiment. The error bars indicate the standard deviation. 30 droplets were evaluated for each data point. Experiments were performed with the standard parameters defined in Sec. III C for both PS and yeast, except for the concentration, which was lower for yeast. Yeast cells can be separated more efficiently than PS particles. This might be due to the lower concentration.

TABLE I. Single particle (P) separation efficiencies at increasing droplet flow speeds. At a droplet (Drop) speed of 2 mm/s, no particle escapes into the side outlet. Even at droplet speeds of around 8 mm/s, a mean single yeast SE above 77% can be maintained. As in Fig. 4, the manipulation of yeast cells is even more efficient than of PS beads.

Speed (mm s ⁻¹)	Drop/min (#)	Drop volume (nl)	Particle	Split ratio (%)	ppd (#)	Drop with 1 particle	P to side	Side/total	Ø SE (%)
2.06	114.3 ± 2.1	12.2 ± 0.2	PS	42.4 ± 0.1	0.63 ± 0.77	162	0	0	100
			Yeast	41 ± 0.6	1.24 ± 1.48	36	0	0	100
4.12	231 ± 0.8	12.12 ± 0.04	PS	41.0 ± 0.6	0.79 ± 0.92	203	17	0.08	91.6
			Yeast	48.6 ± 0.1	0.8 ± 0.87	102	4	0.04	96.1
5.49	327.5 ± 5	11.46 ± 0.12	PS	44.4 ± 0.5	0.69 ± 0.9	135	27	0.20	80
			PS	45.8 ± 0.5	0.64 ± 0.76	171	67	0.39	60.82
8.24	532.1 ± 15.4	10.53 ± 0.3	PS	49 ± 0.11	0.48 ± 0.71	126	29	0.23	77
			Yeast						

Sec. IV C, the separation efficiency decreased for higher droplet flow speeds due to the increasing effect of intra-droplet flow fields. Compared to PS beads, yeast cells exhibit a higher SE, as has been demonstrated in Sec. IV D. Nevertheless, at a flow speed of 8.2 mm s⁻¹, which corresponds to a throughput of 8.9 droplets per second, our approach still achieved an average yeast cell SE of 77%. In comparison to current acoustofluidic intra-droplet particle separation, this result demonstrates a significant improvement with the potential to further enhance the applicability of acoustofluidic systems for biomedical as well as the pharmaceutical industry. Notably, single-particle SE is significantly higher than that for several particles. This might be due to the more confined movement of the particles in the tip of the droplets (Video 5 in the supplementary material).

F. HeLa and bacteria manipulation inside droplets

In this section, we present experimental results for the successful manipulation of HeLa cells and *E. coli* bacteria, both of which have not been manipulated in nanoliter droplets previously.

HeLa cells, like yeast cells, exhibit acoustic properties similar to PS but are larger than the used PS particles (15 μm diameter).⁴⁹

As can be seen in Fig. 5(a), HeLa cells can be manipulated by the ARF inside nanoliter droplets. We used the standard parameters except for the concentration, which was changed to 4.4 ± 2.2 cells per droplet. The cells gather in the tip of the droplet just as the PS particles and the yeast cells. As in Sec. IV C, we counted 30 droplets and attained a separation efficiency of 88.4% ± 11.6%. In further experiments, we increased the cell concentration. However, even at slightly higher concentrations, HeLa cell supernatant adhered along the channel walls and impeded the droplet production, and thereby, also the cell separation (Video 7 in the supplementary material). We believe that this adhesion occurred due to an inappropriate channel coating. For higher HeLa cell concentrations, a biocompatible channel coating needs to be utilized that impedes the adhesion of unwanted cell material.

E. coli have a density close to PS, but neither the compressibility nor the speed of sound is well explored.⁵⁰ The bacteria are much smaller (1 μm length, 0.5 μm diameter) than the used PS particles. The critical particle radius for acoustic manipulation at an excitation frequency of 4 MHz is around 0.7 μm due to acoustic streaming. Furthermore, the acoustic properties of *E. coli* are not well known. Thus, the application of acoustic particle manipulation

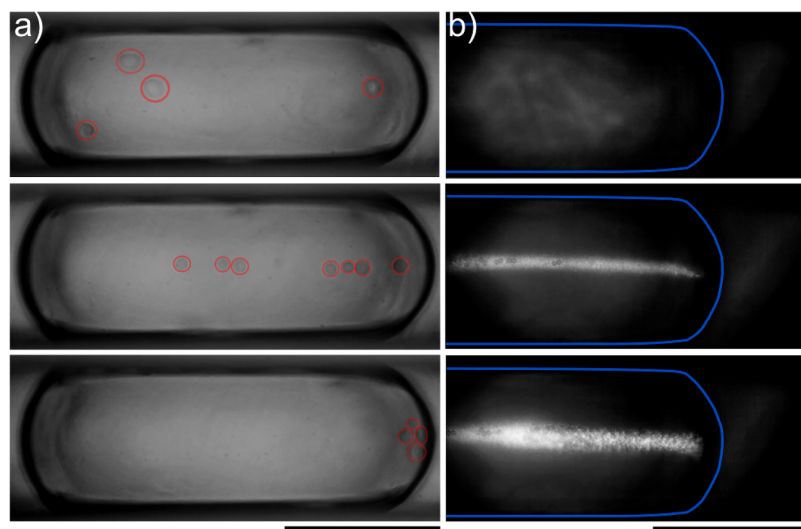


FIG. 5. Micrographs of cell focusing experiments of HeLa and *E. coli*. (a) Low concentrations of HeLa cells (4.4 ± 2.2 cells per droplet) were successfully manipulated at a frequency of 3.75 MHz in 12.8 ± 1.2 nl droplets flowing with a speed of 2 mm s⁻¹. (b) At a low droplet speed of 0.2 mm s⁻¹, it has been possible to manipulate *E. coli* bacteria with the same frequency as for the HeLa cells. The droplet is outlined in blue. The bacteria strain was modified such that they are fluorescent and, therefore, visible, here as a bright cloud, when they reach a sufficient concentration. The concentration was ~4800 bacteria/droplet. Scale bars corresponding to 180 μm.

for *E. coli* is challenging.⁵¹ We used a modified *E. coli* MG1655 strain with a chromosomal copy of the green fluorescent protein mNeonGreen under a constitutive promoter to be able to observe the bacteria. Therefore, just as the PS particles, the bacteria appear as bright dots in the filtered microscope images. The approximate concentration was 4800 bacteria per droplet. As can be seen in Fig. 5(b), it was possible to move the bacteria to the center of the droplet. We believe that this was possible due to rotating streaming flows that only appear in square-shaped channels.⁴⁴ However, the speed of the droplet shown here was slow (0.2 mm s^{-1}) to reduce the strength of the internal flow fields. At such low flow speeds, the droplets cannot be split at the bifurcation due to surface tension as discussed in Sec. II. When increasing the droplet speed, manipulation of the bacteria is not possible anymore. Therefore, splitting the droplets into a bacteria-containing and an empty droplet could not be achieved in the current chip configuration.

Given the presented challenges, further investigations are required for the reliable intra-droplet manipulation and separation of *E. coli* bacteria and HeLa cells. Nevertheless, our approach demonstrates the considerable potential for the manipulation of various cell types, which broadens the field of acoustofluidics and enables progressive interdisciplinary research.

V. CONCLUSION AND OUTLOOK

In this work, we presented an acoustofluidic chip capable of single-particle manipulation inside nanoliter droplets. We characterized the design and proposed general design criteria. Bifurcation angles of 45° exhibit sharp edge-like structures, which lead to particle attraction. To avoid this attraction, edges should be rounded off or different designs should be chosen. To obtain a homogeneous acoustic field, the side channel should be produced as small as possible. However, below a width of $90 \mu\text{m}$, droplet splitting was difficult to control.

Characterizing experiments showed that the speed of the droplets has a huge influence on the separation efficiency due to the internal flow fields. A smaller droplet volume and a lower split ratio led to increased separation efficiency. In 8 nl droplets at a speed of 4 mm s^{-1} , we achieved an average separation efficiency of 99.5%. Compared to current acoustic-based intra-droplet separation, this represents an increase in separation efficiency while doubling the flow speed and decreasing the droplet volume. This improvement is especially crucial for rare cell separation. For a high concentration of more than 900 particles per droplet, we achieved, on average, high separation efficiencies of above 97%. Furthermore, we analyzed the influence of the split ratio. Lowering the split ratio can substantially increase the separation efficiency allowing for improved throughput capabilities.

In the next step, we replaced the PS particles used throughout the characterization process with yeast cells, which are of broad interest for biology-related groups. Yeast cells have similar acoustophoretic mobilities to $5 \mu\text{m}$ PS particles and thus can be separated with a high SE. If the cell concentration is reduced to the single-cell level, SE of 100% can be achieved at a throughput of 114.3 ± 2.1 droplets per minute. Our novel results highlight the significant potential of acoustofluidic intra-droplet manipulation of individual

cells and possibly represent an important step towards advanced applications such as directed evolution.

Finally, we tested the manipulation of HeLa cells and *E. coli* bacteria in nanoliter droplets. Even though the separation of these cells proved to be challenging, the first manipulation of bacteria and mammalian cells inside nanoliter droplets might be of considerable importance for biomedical research.

In the future, the device will be integrated into a screening platform and combined with mass spectrometry to analyze the cell supernatant. We believe that the method is useful for other applications and analytical methods, e.g., to distinguish intracellular and extracellular compounds or retrieve cell products.

SUPPLEMENTARY MATERIAL

See the supplementary material for (1) experimental video of polystyrene particle manipulation corresponding to Fig. 1(c); (2) particle separation at a 45° bifurcation; (3) particle focusing in rectangular microchannels; (4) high particle concentration separation; (5) yeast cell separation in nanoliter droplets corresponding to Fig. 4(a); (6) single PS particle separation corresponding to Table I (row 1); (7) single yeast cell separation corresponding to Table I (row 2); (8) single yeast cell separation corresponding to Table I (row 4); and (9) device contamination due to HeLa cells.

ACKNOWLEDGMENTS

The authors would like to express their gratitude for funding by ETH Zurich and acknowledge support by the ETHZ Bioprocess Laboratory for providing the *E. coli* bacteria as well as the ETHZ Macromolecular Engineering Laboratory for providing the HeLa cells. Finally, the authors would like to thank Agnieszka Ladosz for support with the initial design idea.

The authors declare no competing financial interest.

DATA AVAILABILITY

The data that support the findings of this study are available within the article and its supplementary material. The simulation model is available from the corresponding author upon request.

REFERENCES

- D. Hümmer, F. Kurth, N. Naredi-Rainer, and P. S. Dittrich, *Lab Chip* **16**, 447 (2016).
- N. Shembekar, H. Hu, D. Eustace, and C. A. Merten, *Cell Rep.* **22**, 2206 (2018).
- P. Shahi, S. C. Kim, J. R. Haliburton, Z. J. Gartner, and A. R. Abate, *Sci. Rep.* **7**, 1 (2017).
- T. Konry, M. Dominguez-Villar, C. Baecher-Allan, D. A. Hafler, and M. L. Yarmush, *Biosens. Bioelectron.* **26**, 2707 (2011).
- K. Eyer, R. C. L. Doineau, C. E. Castrillon, L. Briseño-Roa, V. Menrath, G. Mottet, P. England, A. Godina, E. Brient-Litzler, C. Nizak, A. Jensen, A. D. Griffiths, J. Bibette, P. Bruhns, and J. Baudry, *Nat. Biotechnol.* **35**, 977 (2017).
- J. J. Agresti, E. Antipov, A. R. Abate, K. Ahn, A. C. Rowat, J. C. Baret, M. Marquez, A. M. Klibanov, A. D. Griffiths, and D. A. Weitz, *Proc. Natl. Acad. Sci. U.S.A.* **107**, 4004 (2010).
- A. Fallah-Araghi, J. C. Baret, M. Ryckelynck, and A. D. Griffiths, *Lab Chip* **12**, 882 (2012).

- ⁸B. Kintses, C. Hein, M. F. Mohamed, M. Fischlechner, F. Courtois, C. Lainé, and F. Hollfelder, *Chem. Biol.* **19**, 1001 (2012).
- ⁹L. Mahler, K. Wink, R. J. Beulig, K. Scherlach, M. Tovar, E. Zang, K. Martin, C. Hertweck, D. Belder, and M. Roth, *Sci. Rep.* **8**, 1 (2018).
- ¹⁰A. Ali-Cherif, S. Begolo, S. Descroix, J. L. Viovy, and L. Malaquin, *Angew. Chem. Int. Ed.* **51**, 10765 (2012).
- ¹¹E. Brouzes, T. Kruse, R. Kimmerling, and H. H. Strey, *Lab Chip* **15**, 908 (2015).
- ¹²D. Lombardi and P. S. Dittrich, *Anal. Bioanal. Chem.* **399**, 347 (2011).
- ¹³S. I. Han, H. Soo Kim, and A. Han, *Biosens. Bioelectron.* **97**, 41 (2017).
- ¹⁴M. Hein, M. Moskopp, and R. Seemann, *Lab Chip* **15**, 2879 (2015).
- ¹⁵M. Sun, Z. S. Khan, and S. A. Vanapalli, *Lab Chip* **12**, 5225 (2012).
- ¹⁶G. K. Kurup and A. S. Basu, *Biomicrofluidics* **6**, 1 (2012).
- ¹⁷S. Oberti, A. Neild, R. Quach, and J. Dual, *Ultrasonics* **49**, 47 (2009).
- ¹⁸G. Destgeer, H. Cho, B. H. Ha, J. H. Jung, J. Park, and H. J. Sung, *Lab Chip* **16**, 660 (2015).
- ¹⁹Z. Liu, A. Fornell, L. Barbe, K. Hjort, and M. Tenje, *Biomicrofluidics* **13**, 64123 (2019).
- ²⁰X. Qin, H. Wang, and X. Wei, *RSC Adv.* **10**, 11565 (2020).
- ²¹A. Fornell, Z. Liu, and M. Tenje, *Microelectron. Eng.* **226**, 111303 (2020).
- ²²A. Fornell, J. Nilsson, L. Jonsson, P. K. Periyannan Rajeswari, H. N. Joensson, and M. Tenje, *Anal. Chem.* **87**, 10521 (2015).
- ²³J. H. Jung, G. Destgeer, B. Ha, J. Park, and H. J. Sung, *Lab Chip* **16**, 3235–3243 (2016).
- ²⁴G. Destgeer, J. H. Jung, J. Park, H. Ahmed, and H. J. Sung, *Anal. Chem.* **89**, 736 (2016).
- ²⁵K. Park, J. Park, J. H. Jung, G. Destgeer, H. Ahmed, and H. J. Sung, *Biomicrofluidics* **11**, 64112 (2017).
- ²⁶A. Fornell, M. Ohlin, F. Garofalo, J. Nilsson, and M. Tenje, *Biomicrofluidics* **11**, 031101 (2017).
- ²⁷A. Fornell, K. Cushing, J. Nilsson, M. Tenje, A. Fornell, K. Cushing, J. Nilsson, and M. Tenje, *Appl. Phys. Lett.* **112**, 63701 (2018).
- ²⁸J. Park, G. Destgeer, H. Kim, Y. Cho, and H. J. Sung, *Lab Chip* **18**, 2936 (2018).
- ²⁹A. Fornell, F. Garofalo, J. Nilsson, H. Bruus, and M. Tenje, *Microfluid. Nanofluidics* **22**, 75 (2018).
- ³⁰M. A. Saucedo-Espinosa and P. S. Dittrich, *Anal. Chem.* **92**, 8414 (2020).
- ³¹M. Tenje, A. Fornell, M. Ohlin, and J. Nilsson, *Anal. Chem.* **90**, 1434 (2018).
- ³²T. Laurell and A. Lenshof, *Microscale Acousto Fluidics* (The Royal Society of Chemistry, 2015).
- ³³C. W. Shields, K. A. Ohiri, L. M. Szott, and G. P. López, *Cytometry Part B* **92B**, 115–125 (2017).
- ³⁴M. Wiklund, *Lab Chip* **12**, 2018 (2012).
- ³⁵H. Liu and Y. Zhang, *J. Appl. Phys.* **106**, 34906 (2009).
- ³⁶G. F. Christopher, N. N. Noharuddin, J. A. Taylor, and S. L. Anna, *Phys. Rev. E* **78**, 1 (2008).
- ³⁷V. van Steijn, M. T. Kreutzer, and C. R. Kleijn, *Chem. Eng. Sci.* **62**, 7505 (2007).
- ³⁸P. Garstecki, M. J. Fuerstman, H. a Stone, and G. M. Whitesides, *Lab Chip* **6**, 437 (2006).
- ³⁹C. N. Baroud, F. Gallaire, and R. Dangla, *Lab Chip* **10**, 2032 (2010).
- ⁴⁰L. Gorkov, *Phys.-Dokl.* **6**, 773 (1962).
- ⁴¹A. D. Pierce, *Acoustics: An Introduction to Its Physical Principles and Applications* (Woodbury, 1991).
- ⁴²Z. Liu, L. Zhang, Y. Pang, X. Wang, and M. Li, *Microfluid. Nanofluidics* **21**, 1 (2017).
- ⁴³H. Kinoshita, S. Kaneda, T. Fujii, and M. Oshima, *Lab Chip* **7**, 338 (2007).
- ⁴⁴M. Antfolk, P. B. Muller, P. Augustsson, H. Bruus, and T. Laurell, *Lab Chip* **14**, 2791 (2014).
- ⁴⁵A. Carlson, M. Do-Quang, and G. Amberg, *Int. J. Multiph. Flow* **36**, 397 (2010).
- ⁴⁶Y. Wang, M. Do-Quang, and G. Amberg, *Phys. Fluids* **28**, 33103 (2016).
- ⁴⁷A. A. Doinikov, M. S. Gerlt, and J. Dual, *Phys. Rev. Lett.* **124**, 154501 (2020).
- ⁴⁸W. W. Baldwin and H. E. Kubitschek, *J. Bacteriol.* **158**, 701 (1984).
- ⁴⁹E. C. Weiss, P. Anastasiadis, G. Pilarczyk, R. M. Lemor, and P. V. Zinin, *IEEE Trans. Ultrason. Ferroelectr. Freq. Control* **54**, 2257 (2007).
- ⁵⁰W. W. Baldwin, R. Myer, N. Powell, E. Anderson, and A. L. Koch, *Arch. Microbiol.* **164**, 155–157 (1995).
- ⁵¹H. Bruus, *Lab Chip* **12**, 1578 (2012).